

# Distance effect of single atoms on the stability of cobalt oxide catalysts for acidic oxygen evolution

Zhirong Zhang<sup>1†</sup>, Chuanyi Jia<sup>2†</sup>, Peiyu Ma<sup>3†</sup>, Chen Feng<sup>1</sup>, Jiana Zheng<sup>1</sup>, Jin Yang<sup>1</sup>, Junming Huang<sup>1</sup>, Ming Zuo<sup>1</sup>, Shiming Zhou<sup>1\*</sup>, Jie Zeng<sup>1,4\*</sup>

## Abstract

Developing efficient and economical electrocatalysts for acidic oxygen evolution reaction (OER) is essential for proton exchange membrane water electrolyzers (PEMWE). Cobalt oxides are considered promising non-precious OER catalysts due to their high activities. However, the severe dissolution of Co atoms in acid media leads to the collapse of crystal structure, which impedes their application in PEMWE. Here, we reported that introducing acid-resistant Ir single atoms into the lattice of spinel cobalt oxides can significantly suppress the Co dissolution and keep them highly stable during the acidic OER process. Combining theoretical and experimental studies, we revealed that the stabilizing effect induced by Ir heteroatoms exhibited a strong dependence on the distance of adjacent Ir single atoms, where the OER stability of cobalt oxides was continuously improved with decreasing the distance. When the distance was reduced to about 0.6 nm, the spinel cobalt oxides presented no obvious degradation over a 60-hour stability test for acidic OER, suggesting potential for practical applications.

## Introduction

Proton exchange membrane water electrolysis (PEMWE) driven by renewable electricity is the most promising route to the production of clean hydrogen fuels (1, 2). The large-scale deployment of PEMWE devices is predominantly obstructed by the efficient catalysts for oxygen evolution reaction (OER) in acidic media. Currently, precious metal oxide IrO<sub>2</sub> is generally considered to be the most stable electrocatalyst for the acidic OER (3, 4). However, the serious scarcity of iridium, with global production of only about 7 tons per year, makes it difficult for PEMWE to reach sustainable terawatt level goals, where more than 40 years of annual iridium production are estimated to be required (5, 6). Therefore, it is highly desired but remains a major challenge, to develop efficient and durable catalysts with low precious metal consumption for acidic OER.

Cobalt oxides are regarded as a very promising candidate for catalyzing OER due to their earth abundance and excellent activity (7-10). In particular, spinel cobalt oxides attract extensive attention benefiting from their flexible composition and tunable structure (11, 12). Nevertheless, these oxides are only stable during the OER process in neutral or alkaline media. Under acidic conditions, the dissolution of cobalt atoms leads to the collapse of crystal structure, which limited their application in PEMWE (13-15). Recently, some pioneering works have reported that the introduction of acid-resistant heteroatoms such as Pb, Mn, and Sb into cobalt oxides could increase the stability of these OER catalysts in acid (6, 11, 16, 17). It was proposed that the heteroatoms would strengthen metal-oxygen bindings (6), activate the self-healing process (16), or stabilize the lattice (17). However, atomic-level insight into the stabilizing effect induced by the acid-resistant heteroatoms is still lacking, which is crucial for designing highly efficient earth-abundant catalysts for acidic OER.

Herein, combining theoretical and experimental studies on single-atom Ir-introduced spinel cobalt oxides, we provided an in-depth understanding of the heteroatom's role on OER stability at the atomic level. Our density functional theory (DFT) calculations revealed that the introduction of Ir single atoms can significantly increase the migration energy of the nearest Co atoms, whereas has less influence on the distant ones. Accordingly, we further studied the inter-site distance effect of adjacent Ir atoms, i.e., Ir-Ir distance, on the stability of Co atoms between them. We found that the stability of the in-between Co atom was continuously enhanced until the Ir-Ir distance was lowered down to the limited level of 0.56 nm where the Co atom was sandwiched by two Ir atoms. Experimentally, we successfully synthesized a series of single-atom catalysts with different Ir-Ir distances by adjusting the density of Ir single atoms in spinel cobalt oxides. Electrochemical measurements further demonstrated that the stabilizing effect induced by Ir single atoms was closely related to the Ir-Ir distance. With the decrease of the Ir-Ir distance, the electrochemical durability of these catalysts in acid exhibited a gradual improvement, accompanied by a significant decrease in the dissolution of Co species, which well confirmed the theoretical results. When the Ir-Ir distance reached about 0.6 nm, the long-term durability test at  $10 \text{ mA cm}_{\text{geo}}^{-2}$  revealed that the spinel cobalt oxide remained stable under  $\text{pH} = 1$  with just a small increase in the potential of about 20 mV after a 60 h continuous operation. Our work offered essential guidance for the precise design of highly stable earth-abundant OER catalysts in acid media.

## Exploration of the distance-related stabilizing effect

We began with DFT calculations to study how the introduction of acid-resistant heteroatoms influences the stability of Co atoms in spinel oxides. Since the dissolution of cobalt oxides in acid involves the migration of Co atoms at the surface (6, 18), we calculated the migration energies of these lattice atoms to evaluate their stabilities. Taking spinel  $\text{Cu}_{0.3}\text{Co}_{2.7}\text{O}_4$  as a model (Fig. 1A), we proposed a migrating process of the Co atom at octahedral sites as shown in Fig. 1B, where the Co atom moves away from the (110) face via a transition state with an energy barrier of 1.58 eV. After Ir single atoms were introduced into the octahedral sites of spinel oxide (Fig. 1C), we first calculated the migration energy of the nearest Co atom (labeled as A) to the Ir single atom. We found that the energy increased to 1.70 eV (Fig. S1A), indicating that the introduction of the Ir single atom can significantly enhance the stability of the nearest Co atom. Subsequently, we further assessed the influence of Ir single atom on the migration of distant Co atoms, i.e., the next nearest Co atom as labeled B in Fig. 1C. The calculated migration energy of B-site Co was 1.63 eV (Fig. S1B), which suggested that the B-site Co atom was less stable than the A-site Co but more than the Co atom without introducing Ir (Fig. 1D). In other words, the stabilizing effect induced by Ir single atoms became weaker as the distance between Ir and Co atoms increased. This result strongly suggested that it is necessary to control the distance of adjacent Ir single atoms by adjusting the density of introduced Ir single atoms for improving the stability of the cobalt oxide catalysts.

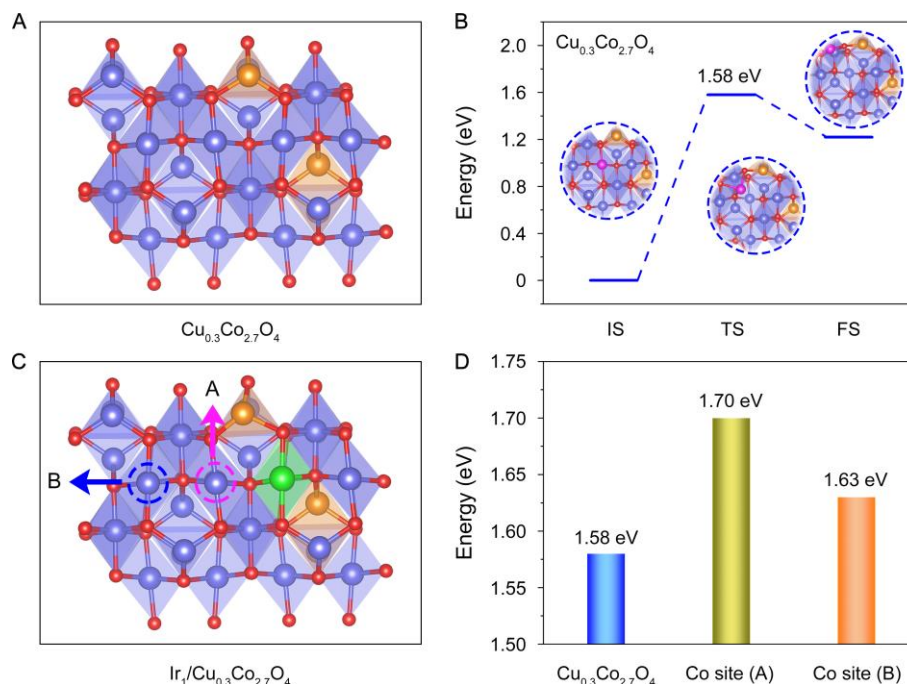


**Fig. 1. Optimized structural models and calculated migration energies of Cu<sub>0.3</sub>Co<sub>2.7</sub>O<sub>4</sub> and Ir<sub>1</sub>/Cu<sub>0.3</sub>Co<sub>2.7</sub>O<sub>4</sub>.** (A) Optimized structural model of Cu<sub>0.3</sub>Co<sub>2.7</sub>O<sub>4</sub>. Red, blue, and brown spheres represent O, Co, and Cu atoms, respectively. (B) Calculated migration energies of Co atoms on Cu<sub>0.3</sub>Co<sub>2.7</sub>O<sub>4</sub>. Pink spheres represent migrated Co atoms. (C) Optimized structural model of Ir<sub>1</sub>/Cu<sub>0.3</sub>Co<sub>2.7</sub>O<sub>4</sub>. Green spheres represent the Ir atom. Pink and blue circles represented the Co site located at different distances from the Ir atom. (D) Calculated migration energies of Co atoms at different sites.

To further explore the distance-dependent stabilizing effect of Ir single atoms, we constructed various structural models of Ir atomically doped spinel cobalt oxides, Ir<sub>1</sub>/Cu<sub>0.3</sub>Co<sub>2.7</sub>O<sub>4</sub>, with different Ir-Ir distances (d). Fig. 2A-C showed the cases with d = 1.14, 0.87, and 0.56 nm, in which the number of Co atoms between two adjacent Ir atoms was 3, 2, and 1, respectively. For d = 1.14 nm, the calculated migration energy of the centered Co atom was 1.63 eV. For d = 0.87 nm, the energy was 1.75 eV (Fig. 2D). Both the energies are essentially the same as those for B-site and A-site Co atoms in Fig. 1C, respectively. For d = 0.56 nm, it took 1.83 eV to enable the migration of the Co atom sandwiched by two Ir single atoms (Fig. 2D). The increased migration energies indicated that the shorter the distance between adjacent Ir single atoms, the more stable the Co atoms on the catalyst surface. The above results indicated that Ir single atoms can stabilize their neighboring lattice but have limited effect on distant ones. When the distance between adjacent Ir single atoms was too large, the stabilizing

effect of Ir single atoms was localized. Once the distance between Ir single atoms was reduced to a specific value, the stabilizing effect would cover the spinel oxides effectively, thus stabilizing the entire spinel oxides under acidic conditions (Fig. 2E).

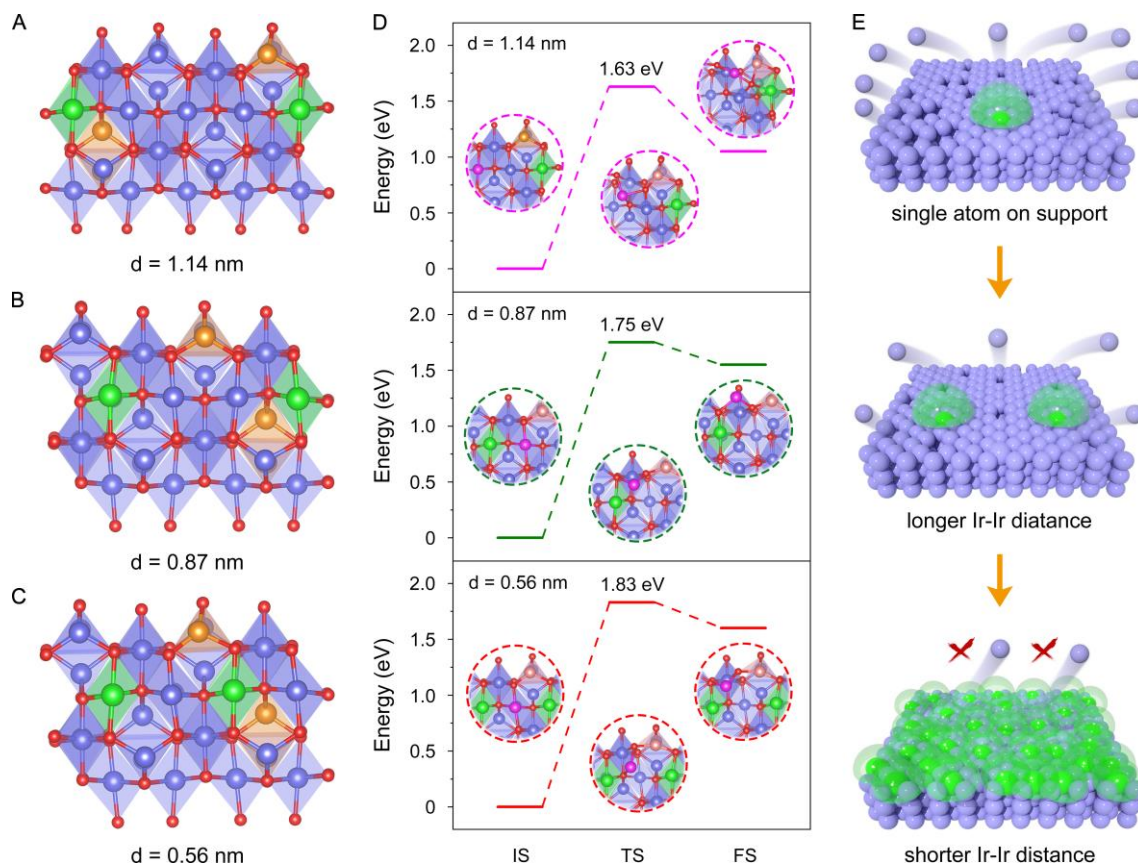


**Fig. 2. Optimized structural models and calculated migration energies of Ir<sub>1</sub>/Cu<sub>0.3</sub>Co<sub>2.7</sub>O<sub>4</sub> with different Ir-Ir distances.** (A, B, C) Optimized structural models of Ir<sub>1</sub>/Cu<sub>0.3</sub>Co<sub>2.7</sub>O<sub>4</sub> with different Ir-Ir distances. Ir<sub>1</sub>/Cu<sub>0.3</sub>Co<sub>2.7</sub>O<sub>4</sub> with d = 1.14 nm (A), d = 0.87 nm (B), and d = 0.56 nm (C). Red, blue, brown, and green spheres represent O, Co, Cu, and Ir atoms, respectively. (D) Calculated migration energies of Co atoms on Ir<sub>1</sub>/Cu<sub>0.3</sub>Co<sub>2.7</sub>O<sub>4</sub> with different Ir-Ir distances. The inset structures represent the initial state (IS), transition state (TS), and final state (FS), respectively. Pink spheres represent migrated Co atoms. (E) Schematic illustration of the distance effect of Ir single atoms on the stability of cobalt oxide catalysts. Blue and green spheres represent Co atoms and Ir single atoms.



## Identifying $\text{Ir}_1/\text{Cu}_{0.3}\text{Co}_{2.7}\text{O}_4$ with different Ir single atoms distance

Inspired by the theoretical calculations, we synthesized spinel oxide  $\text{Cu}_{0.3}\text{Co}_{2.7}\text{O}_4$  and a series of  $\text{Ir}_1/\text{Cu}_{0.3}\text{Co}_{2.7}\text{O}_4$  with different Ir-Ir distances through a high-temperature pyrolysis method (see Methods). The distance between Ir single atoms was modulated by adjusting the density of Ir single atoms on  $\text{Cu}_{0.3}\text{Co}_{2.7}\text{O}_4$ . Transmission electron microscopy (TEM) images showed that the as-prepared  $\text{Cu}_{0.3}\text{Co}_{2.7}\text{O}_4$  and  $\text{Ir}_1/\text{Cu}_{0.3}\text{Co}_{2.7}\text{O}_4$  with different Ir-Ir distances presented similar morphologies (Fig. S2). X-ray diffraction (XRD) patterns revealed that all the samples were in the spinel-type structures with a  $Fd-3m$  space group (Fig. S3). Moreover, the Raman spectra displayed four characteristic peaks located at 190, 470, 510, and 682  $\text{cm}^{-1}$  for these oxides, which were assigned to  $F_{2g}$ ,  $E_g$ ,  $F_{2g}$ , and  $A_{1g}$  vibration originated from the spinel lattice, respectively (Fig. S4) (ref.<sup>11, 19</sup>). These results demonstrated that the introduction of Ir heteroatoms into the spinel cobalt oxides not only formed no detectable impurity phase but also unchanged the spinel structure.

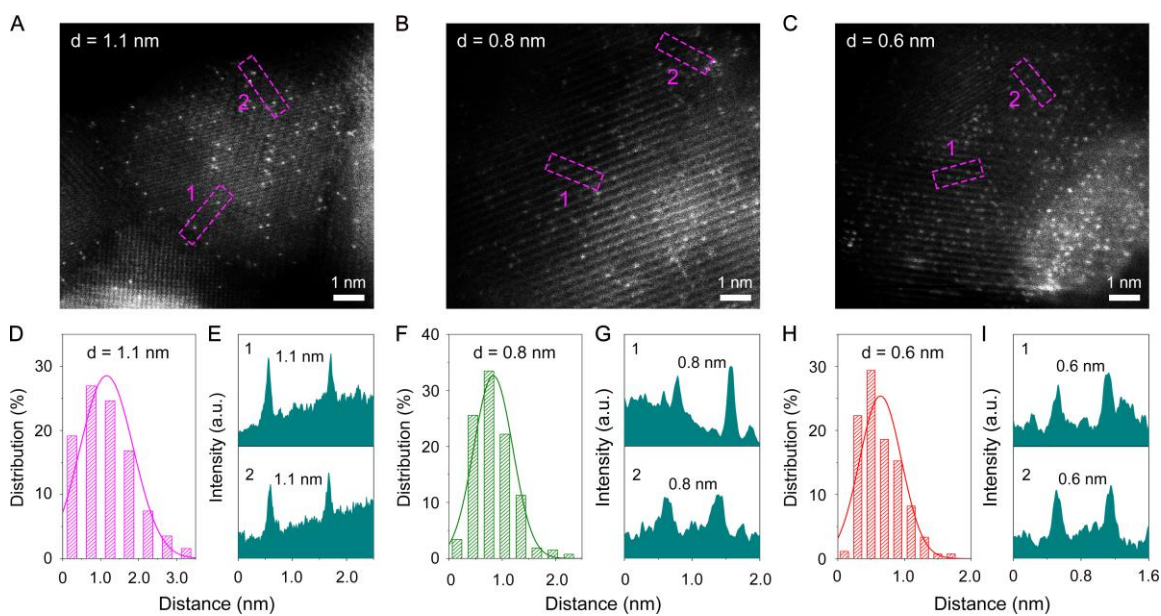


**Fig. 3. Structural characterizations of  $\text{Ir}_1/\text{Cu}_{0.3}\text{Co}_{2.7}\text{O}_4$  with different Ir-Ir distances.** (A, B, C) HAADF-STEM images of  $\text{Ir}_1/\text{Cu}_{0.3}\text{Co}_{2.7}\text{O}_4$  with different Ir-Ir distances.  $\text{Ir}_1/\text{Cu}_{0.3}\text{Co}_{2.7}\text{O}_4$  with  $d = 1.1$  nm (A),  $d = 0.8$  nm (B), and  $d = 0.6$  nm (C). (D, E) Distance distribution of Ir single atoms (D) and intensity profile (E) of atoms located at the square frame in A. (F, G) Distance distribution of Ir single atoms (F) and intensity profile (G) of atoms located at the square frame in B. (H, I) Distance distribution of Ir single atoms (H) and intensity profile (I) of atoms located at the square frame in C.

Fig. 3A-C showed the aberration-corrected high-angle annular dark-field scanning TEM (HAADF-STEM) images for three  $\text{Ir}_1/\text{Cu}_{0.3}\text{Co}_{2.7}\text{O}_4$  samples with different Ir-Ir distances. Individual bright spots in contrast to the support were found, which indicated that the Ir species were atomically dispersed in the spinel cobalt oxides. Moreover, by averaging the Ir-Ir distances of more than two hundred Ir-Ir pairs in the HAADF-STEM images, the value of  $d$  was estimated to be about 1.1, 0.8, and 0.6 nm, respectively (Fig. 3D-I). Energy dispersive X-ray (EDX) elemental mapping images revealed that the Ir atoms were uniformly distributed in all three  $\text{Ir}_1/\text{Cu}_{0.3}\text{Co}_{2.7}\text{O}_4$  samples (Fig. S5). The quantitative analysis by inductively coupled plasma-atomic emission spectrometry (ICP-AES) showed that the contents of Ir elements were 1.2, 2.1, and 3.6 wt% for  $\text{Ir}_1/\text{Cu}_{0.3}\text{Co}_{2.7}\text{O}_4$  with  $d = 1.1, 0.8,$  and  $0.6$  nm, respectively.

The electronic structure and coordination environment of  $\text{Ir}_1/\text{Cu}_{0.3}\text{Co}_{2.7}\text{O}_4$  with different Ir-Ir distances were further characterized by X-ray absorption near-edge spectroscopy (XANES) and extended X-ray absorption fine structure (EXAFS) spectroscopy. The Co  $K$ -edge XANES spectra showed that the absorption edges of  $\text{Ir}_1/\text{Cu}_{0.3}\text{Co}_{2.7}\text{O}_4$  with different Ir-Ir distances overlapped with that of  $\text{Cu}_{0.3}\text{Co}_{2.7}\text{O}_4$ , suggesting similar valence states for Co species in all the oxides (Fig. 4A) (ref.<sup>20, 21</sup>). The Co  $K$ -edge EXAFS spectra presented three similar characteristic peaks at about 1.4, 2.3, and 3.0 Å, corresponding to Co-O,  $\text{Co}_{\text{oct}}\text{-Co}_{\text{oct}}$  (octahedral site), and  $\text{Co}_{\text{tet}}\text{-Co}_{\text{tet}}$  (tetrahedral site) (Fig. 4B) (ref.<sup>22, 23</sup>) which implies that the coordination environment of Co sites exhibited no obvious change after the introduction of Ir single atoms. Moreover, the Co and Cu  $L$ -edge X-ray absorption spectroscopy (XAS) also revealed similar valence states of Co and Cu ions in these as-prepared samples (Fig. S6A) (ref.<sup>24-28</sup>). The above results indicated that no visible changes in the crystal and electronic structures of the cobalt oxides were found after the introduction of Ir single atoms with different distances. Fig. 4C showed the Ir  $L_3$ -edge XANES spectra of  $\text{Ir}_1/\text{Cu}_{0.3}\text{Co}_{2.7}\text{O}_4$  with different Ir-Ir distances, where  $\text{IrO}_2$  and Ir foil were used as references. The intensity of the white line was found to decline gradually with decreasing the Ir-Ir distances, which suggested a decrease in the valence state of Ir species (29, 30). The Ir  $L_3$ -edge EXAFS spectra exhibited two characteristic peaks at about 2.0 Å and 3.0 Å, which were ascribed to first-shell Ir-O coordination and second-shell Ir-Co coordination, respectively (Fig. 4D) (ref.<sup>31, 32</sup>). By fitting the experimental EXAFS spectra, the Ir-O and Ir-Co coordination numbers of  $\text{Ir}_1/\text{Cu}_{0.3}\text{Co}_{2.7}\text{O}_4$  with different Ir-Ir distances were determined to be about six and three, respectively (Fig. S7 and table S1). The fitting results confirmed that the Ir single atoms were

incorporated into the octahedral sites of  $\text{Cu}_{0.3}\text{Co}_{2.7}\text{O}_4$ .

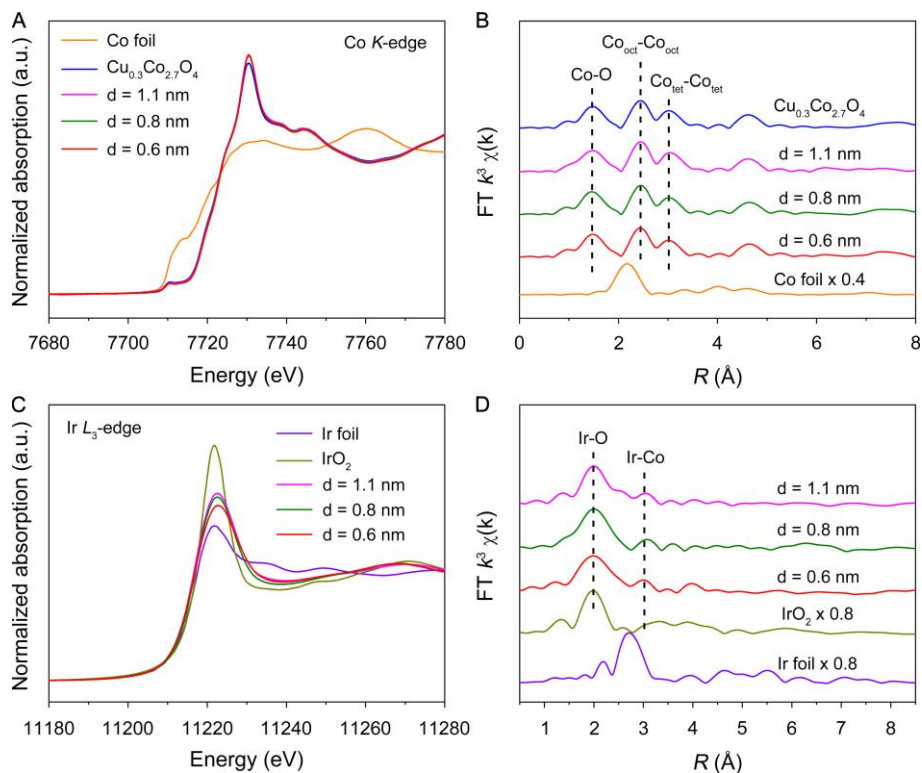


**Fig. 4. Electronic structure characterizations of  $\text{Ir}_1/\text{Cu}_{0.3}\text{Co}_{2.7}\text{O}_4$  with different Ir-Ir distances. (A, B)** Normalized XANES (A) and EXAFS (B) spectra at the Co  $K$ -edge of  $\text{Cu}_{0.3}\text{Co}_{2.7}\text{O}_4$  and  $\text{Ir}_1/\text{Cu}_{0.3}\text{Co}_{2.7}\text{O}_4$  with different Ir-Ir distances. Co foil was used as a reference. (C, D) Normalized XANES (C) and EXAFS spectra (D) at the Ir  $L_3$ -edge of  $\text{Ir}_1/\text{Cu}_{0.3}\text{Co}_{2.7}\text{O}_4$  with different Ir-Ir distances. Ir foil and  $\text{IrO}_2$  were used as references.

## Electrocatalytic evaluation towards acidic oxygen evolution

To evaluate the stabilizing effect of Ir single atoms with different distances on  $\text{Cu}_{0.3}\text{Co}_{2.7}\text{O}_4$ , we recorded the polarization curves under acidic OER (33-35). For the pristine  $\text{Cu}_{0.3}\text{Co}_{2.7}\text{O}_4$ , the current density showed an obvious decrease as the number of scans increased (Fig. 5A). After 1000 scan cycles, the current density decreased by 92.4%. As Ir single atoms with  $d = 1.1$  and  $0.8$  nm were introduced into  $\text{Cu}_{0.3}\text{Co}_{2.7}\text{O}_4$ , the current density decreased by 75.2% and 44.3% after 1000 scan cycles, respectively (Fig. 5A and B). When the Ir-Ir distance was further reduced to  $0.6$  nm, the current density showed an inconspicuous decrease during the sequential scans, indicating excellent OER stability for this sample in acidic media (Fig. 5A and B). The dissolution of Co species under different scan cycles was also measured by ICP-AES to explore



the stability of  $\text{Cu}_{0.3}\text{Co}_{2.7}\text{O}_4$  and  $\text{Ir}_1/\text{Cu}_{0.3}\text{Co}_{2.7}\text{O}_4$  with  $d = 0.6$  nm. For  $\text{Cu}_{0.3}\text{Co}_{2.7}\text{O}_4$ , the Co species were gradually dissolved with increasing the number of scan cycles. Specifically, 76.7% of Co species were dissolved after 1000 scan cycles (Fig. 5C). The dissolution of Co species reduced the number of active sites, which led to a significant decrease in the performance of the catalyst. In contrast, the Co species in  $\text{Ir}_1/\text{Cu}_{0.3}\text{Co}_{2.7}\text{O}_4$  with  $d = 0.6$  nm were merely dissolved (just 3.6%) after 1000 scan cycles, indicating its high stability (Fig. 5C). Long-term chronopotentiometry at a constant current density of  $10 \text{ mA cm}^{-2}_{\text{geo}}$  were also carried out to estimate the durability of  $\text{Cu}_{0.3}\text{Co}_{2.7}\text{O}_4$  and  $\text{Ir}_1/\text{Cu}_{0.3}\text{Co}_{2.7}\text{O}_4$  with different Ir-Ir distances. As shown in Fig. 5D, the durability of these catalysts was improved as the Ir-Ir distance decreased. For  $d = 0.6$  nm, the catalyst remained stable with just a small increase in the potential of about 20 mV after a 60 h continuous operation.

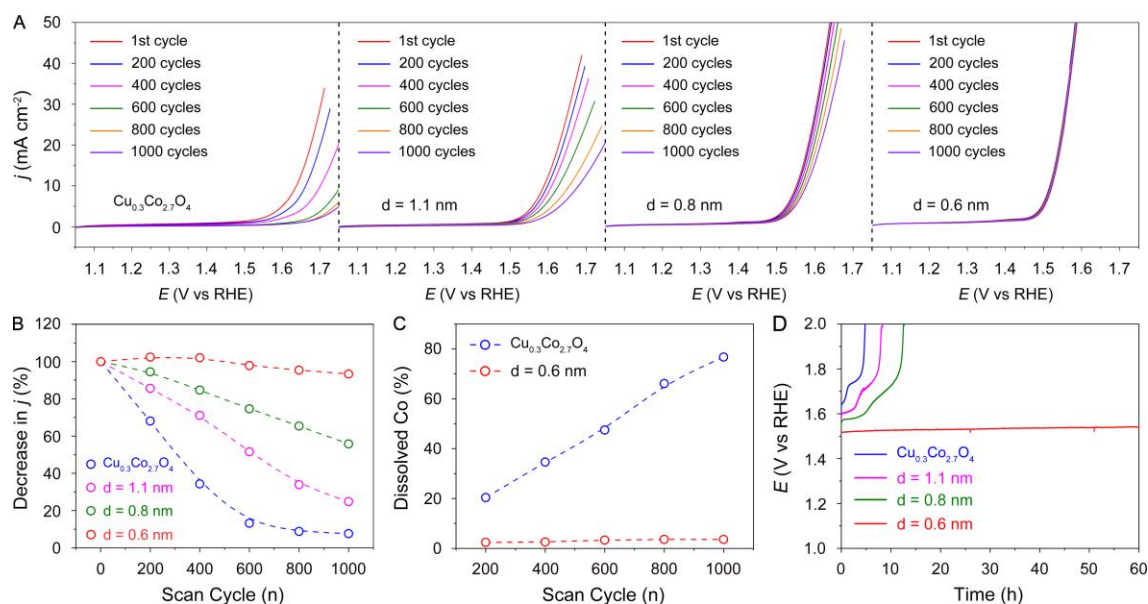


**Fig. 5. Stability evaluation towards acidic oxygen evolution.** (A) Polarization curves of catalysts at different scan cycles in 0.1 M  $\text{HClO}_4$  electrolyte. The displayed polarization curves are the 1, 200, 400, 600, 800, and 1000 cycles, respectively. (B) Decrease in current densities under different scan cycles of  $\text{Cu}_{0.3}\text{Co}_{2.7}\text{O}_4$  and  $\text{Ir}_1/\text{Cu}_{0.3}\text{Co}_{2.7}\text{O}_4$  with different Ir-Ir distances. (C) Dissolution of Co species under different scan cycles of  $\text{Cu}_{0.3}\text{Co}_{2.7}\text{O}_4$  and  $\text{Ir}_1/\text{Cu}_{0.3}\text{Co}_{2.7}\text{O}_4$  with  $d = 0.6$  nm. (D) Chronopotentiometry curves of  $\text{Cu}_{0.3}\text{Co}_{2.7}\text{O}_4$  and  $\text{Ir}_1/\text{Cu}_{0.3}\text{Co}_{2.7}\text{O}_4$  with different Ir-Ir distances towards acidic OER at  $10 \text{ mA cm}^{-2}$ .

The excellent stability of  $\text{Ir}_1/\text{Cu}_{0.3}\text{Co}_{2.7}\text{O}_4$  with  $d = 0.6$  nm was also supported by the

HAADF-STEM image, EDX elemental mapping images, and XAS after the durability test. As shown in the HAADF-STEM image, Ir single atoms preserved their isolated dispersion on the support (Fig. S8A). The EDX elemental mapping image showed that Ir species were still evenly distributed across the catalyst (Fig. S8B). The Co  $L_3$ - and  $L_2$ -edge peaks displayed negligible change compared with that before the durability test, suggesting an unchanged valence state of Co (Fig. S8C). In addition, the O  $K$ -edge XAS also showed ignorable changes in the characteristic peaks, indicating a stable structure of the  $\text{Ir}_1/\text{Cu}_{0.3}\text{Co}_{2.7}\text{O}_4$  with  $d = 0.6$  nm during the durability test (Fig. S8D).

To further prove the excellent stability of  $\text{Ir}_1/\text{Cu}_{0.3}\text{Co}_{2.7}\text{O}_4$  with  $d = 0.6$  nm during acidic OER, *in-situ* XAFS were performed. As shown in Fig. S9A, the absorption edge of Co  $K$ -edge XANES spectra for  $\text{Ir}_1/\text{Cu}_{0.3}\text{Co}_{2.7}\text{O}_4$  with  $d = 0.6$  nm exhibited negligible changes with increasing voltage from open circle potential (OCP) to 1.7 V, suggesting the excellent stability of the catalysts under oxidative potentials (33). Meanwhile, the EXAFS spectra revealed that the position and intensity of the three main peaks from the Co-O,  $\text{Co}_{\text{oct}}\text{-Co}_{\text{oct}}$ , and  $\text{Co}_{\text{tet}}\text{-Co}_{\text{tet}}$  coordination exhibited an insignificant change with increasing voltage, indicating a stable structure of this sample during acidic OER (Fig. S9B). These *in-situ* XAFS results demonstrated that Ir single atoms with  $d = 0.6$  nm effectively stabilized the structure of  $\text{Cu}_{0.3}\text{Co}_{2.7}\text{O}_4$  during acidic OER.

The electrocatalytic activity of  $\text{Ir}_1/\text{Cu}_{0.3}\text{Co}_{2.7}\text{O}_4$  with different Ir-Ir distances towards acidic OER was also evaluated. For comparison,  $\text{Cu}_{0.3}\text{Co}_{2.7}\text{O}_4$  was measured under the same conditions. Fig. S10A displayed that the introduction of Ir single atoms improves the OER activity. Moreover, the current density of  $\text{Ir}_1/\text{Cu}_{0.3}\text{Co}_{2.7}\text{O}_4$  increased with decreasing the distance of adjacent Ir single atoms. Specifically,  $\text{Ir}_1/\text{Cu}_{0.3}\text{Co}_{2.7}\text{O}_4$  with  $d = 0.6$  nm only required an overpotential of 290 mV to deliver a current density of  $10 \text{ mA cm}^{-2}$ , which was 120, 70, and 30 mV lower than those of  $\text{Cu}_{0.3}\text{Co}_{2.7}\text{O}_4$ ,  $\text{Ir}_1/\text{Cu}_{0.3}\text{Co}_{2.7}\text{O}_4$  with  $d = 1.1$  and  $0.8$  nm, respectively (Fig. S10B). The results indicated that the reduction of the distance between Ir single atoms significantly enhanced the catalytic activity under the acidic condition. To elucidate the reaction kinetics, we analyzed the Tafel slopes of these catalysts, where the Tafel slope of  $\text{Ir}_1/\text{Cu}_{0.3}\text{Co}_{2.7}\text{O}_4$  with  $d = 0.6$  nm gave the lowest value of  $71 \text{ mV dec}^{-1}$  (Fig. S11). This suggested its fastest kinetics among these catalysts (34). The reaction kinetics was further reflected by the electrochemical impedance spectroscopy (EIS) measurements. A remarkable decrease of charge

transfer resistance ( $R_{ct}$ ) was found in the  $\text{Ir}_1/\text{Cu}_{0.3}\text{Co}_{2.7}\text{O}_4$  with  $d = 0.6$  nm compared with other catalysts, confirming its fastest charge transfer (Fig. S12) (ref.<sup>35, 36</sup>). The improved catalytic performance and accelerated reaction kinetics of  $\text{Ir}_1/\text{Cu}_{0.3}\text{Co}_{2.7}\text{O}_4$  with  $d = 0.6$  nm may be attributed to the optimized electronic structure of Co atoms after the introduction of Ir single atoms.

To test the generality of distance effect on the stability of cobalt oxide catalysts for acidic OER, we further introduced Ir single atoms into other spinel cobalt oxides such as  $\text{Co}_3\text{O}_4$  and  $\text{Mn}_{0.3}\text{Co}_{2.7}\text{O}_4$ . Under similar preparing conditions, we successfully obtained the single-atom catalysts,  $\text{Ir}_1/\text{Co}_3\text{O}_4$  and  $\text{Ir}_1/\text{Mn}_{0.3}\text{Co}_{2.7}\text{O}_4$ , with  $d = 0.6$  nm (TEM, XRD, and HAADF-STEM, Fig. S13-S15). The electrochemical measurements (Fig. S16) revealed that both  $\text{Ir}_1/\text{Co}_3\text{O}_4$  and  $\text{Ir}_1/\text{Mn}_{0.3}\text{Co}_{2.7}\text{O}_4$  also exhibited a high OER stability in acid. This proved that the introduction of Ir single atoms with an appropriate distance into cobalt oxides was a universal strategy to stabilize its structure during acidic OER.

## Discussion

In conclusion, we understand the distance effect of single atoms on the stability of cobalt oxide catalysts for acidic oxygen evolution. Both theoretical calculations and electrocatalytic measurements revealed the stabilizing effect was strongly dependent on the distance of adjacent Ir single atoms. As the distance of adjacent Ir single atoms was reduced to 0.6 nm, the stabilizing effect could cover the  $\text{Cu}_{0.3}\text{Co}_{2.7}\text{O}_4$ , stabilizing entire spinel oxides under acidic conditions. In addition, the introduction of Ir single atoms with an appropriate distance was a universal strategy to stabilize other spinel cobalt oxides during acidic OER. Our work not only provided insight into the distance effect of single atoms on the stability of cobalt oxide catalysts at the atomic level but also pointed toward a direction to the rational design of highly stable catalysts applied in PEMWE.

## Methods

**Chemicals.** Cobalt (II) nitrate hexahydrate ( $\text{Co}(\text{NO}_3)_2 \cdot 6\text{H}_2\text{O}$ ), copper (II) nitrate trihydrate ( $\text{Cu}(\text{NO}_3)_2 \cdot 3\text{H}_2\text{O}$ ), hexadecyl trimethyl ammonium bromide (CTAB), 2-methylimidazole, active carbon, ethanol (EtOH), perchloric acid ( $\text{HClO}_4$ ), Nafion were purchased from Shanghai Chemical Reagent Company. Iridium (IV) chloride hydrate ( $\text{IrCl}_4 \cdot x\text{H}_2\text{O}$ ) was purchased from Aladdin. All chemicals were of analytical grade and used as received without further purification. All aqueous solutions were prepared using deionized water with a resistivity of  $18.2 \text{ M}\Omega \text{ cm}^{-1}$ .

**Synthesis of  $\text{Cu}_{0.3}\text{Co}_{2.7}\text{O}_4$ .**  $\text{Cu}_{0.3}\text{Co}_{2.7}\text{O}_4$  was synthesized through high-temperature pyrolysis of metal-organic frameworks with modifications (37). Typically, 497.7 mg of  $\text{Co}(\text{NO}_3)_2 \cdot 6\text{H}_2\text{O}$ , 70.0 mg of  $\text{Cu}(\text{NO}_3)_2 \cdot 3\text{H}_2\text{O}$ , and 30.0 mg of CTAB were dissolved in 20 mL of  $\text{H}_2\text{O}$  to form solution A. 9.1 g of 2-methylimidazole was dissolved in 140 mL of  $\text{H}_2\text{O}$  to form solution B. The mixed solution was formed by adding solution A to solution B and mixed for 2 hours under magnetic stirring. The resulting solution was centrifuged and washed with EtOH three times to obtain metal-organic frameworks. The product was dried in a vacuum oven overnight. Finally, the above solid was calcined at  $350^\circ\text{C}$  for 4 hours in the air to obtain the desired  $\text{Cu}_{0.3}\text{Co}_{2.7}\text{O}_4$ .

**Synthesis of  $\text{Ir}_1/\text{Cu}_{0.3}\text{Co}_{2.7}\text{O}_4$  with different Ir single atoms distance.**  $\text{Ir}_1/\text{Cu}_{0.3}\text{Co}_{2.7}\text{O}_4$  with different Ir single atoms distances were synthesized using similar procedures as synthesizing  $\text{Cu}_{0.3}\text{Co}_{2.7}\text{O}_4$  except for changing the composition of solution A. For  $\text{Ir}_1/\text{Cu}_{0.3}\text{Co}_{2.7}\text{O}_4$  with  $d = 1.1 \text{ nm}$ , 492.7 mg of  $\text{Co}(\text{NO}_3)_2 \cdot 6\text{H}_2\text{O}$ , 69.3 mg of  $\text{Cu}(\text{NO}_3)_2 \cdot 3\text{H}_2\text{O}$ , 6.7 mg of  $\text{IrCl}_4 \cdot x\text{H}_2\text{O}$ , and 30.0 mg of CTAB were dissolved in 20 mL of  $\text{H}_2\text{O}$  to form solution A. For  $\text{Ir}_1/\text{Cu}_{0.3}\text{Co}_{2.7}\text{O}_4$  with  $d = 0.8 \text{ nm}$ , 487.7 mg of  $\text{Co}(\text{NO}_3)_2 \cdot 6\text{H}_2\text{O}$ , 68.6 mg of  $\text{Cu}(\text{NO}_3)_2 \cdot 3\text{H}_2\text{O}$ , 13.4 mg of  $\text{IrCl}_4 \cdot x\text{H}_2\text{O}$ , and 30.0 mg of CTAB were dissolved in 20 mL of  $\text{H}_2\text{O}$  to form solution A. For  $\text{Ir}_1/\text{Cu}_{0.3}\text{Co}_{2.7}\text{O}_4$  with  $d = 0.6 \text{ nm}$ , 482.7 mg of  $\text{Co}(\text{NO}_3)_2 \cdot 6\text{H}_2\text{O}$ , 67.9 mg of  $\text{Cu}(\text{NO}_3)_2 \cdot 3\text{H}_2\text{O}$ , 20.0 mg of  $\text{IrCl}_4 \cdot x\text{H}_2\text{O}$ , and 30.0 mg of CTAB were dissolved in 20 mL of  $\text{H}_2\text{O}$  to form solution A.

**Synthesis of  $\text{Co}_3\text{O}_4$  and  $\text{Mn}_{0.3}\text{Co}_{2.7}\text{O}_4$ .**  $\text{Co}_3\text{O}_4$  and  $\text{Mn}_{0.3}\text{Co}_{2.7}\text{O}_4$  were synthesized using similar procedures as synthesizing  $\text{Cu}_{0.3}\text{Co}_{2.7}\text{O}_4$  except for changing the composition of solution A. For  $\text{Co}_3\text{O}_4$ , 580.0 mg of  $\text{Co}(\text{NO}_3)_2 \cdot 6\text{H}_2\text{O}$  and 30.0 mg of CTAB were dissolved in 20 mL of  $\text{H}_2\text{O}$  to

form solution A. For  $\text{Mn}_{0.3}\text{Co}_{2.7}\text{O}_4$ , 497.7 mg of  $\text{Co}(\text{NO}_3)_2 \cdot 6\text{H}_2\text{O}$ , 52.9 mg of  $\text{Mn}(\text{NO}_3)_2 \cdot 6\text{H}_2\text{O}$ , and 30.0 mg of CTAB were dissolved in 20 mL of  $\text{H}_2\text{O}$  to form solution A.

**Synthesis of  $\text{Ir}_1/\text{Co}_3\text{O}_4$  and  $\text{Ir}_1/\text{Mn}_{0.3}\text{Co}_{2.7}\text{O}_4$  with  $d = 0.6$  nm.**  $\text{Ir}_1/\text{Co}_3\text{O}_4$  with  $d = 0.6$  nm was synthesized using similar procedures as synthesizing  $\text{Co}_3\text{O}_4$  except for changing the composition of solution A. For  $\text{Ir}_1/\text{Co}_3\text{O}_4$  with  $d = 0.6$  nm, 482.7 mg of  $\text{Co}(\text{NO}_3)_2 \cdot 6\text{H}_2\text{O}$ , 20.0 mg of  $\text{IrCl}_4 \cdot x\text{H}_2\text{O}$ , and 30.0 mg of CTAB were dissolved in 20 mL of  $\text{H}_2\text{O}$  to form solution A.  $\text{Ir}_1/\text{Mn}_{0.3}\text{Co}_{2.7}\text{O}_4$  with  $d = 0.6$  nm were synthesized using similar procedures as synthesizing  $\text{Mn}_{0.3}\text{Co}_{2.7}\text{O}_4$  except for changing the composition of solution A. For  $\text{Ir}_1/\text{Mn}_{0.3}\text{Co}_{2.7}\text{O}_4$  with  $d = 0.6$  nm, 482.7 mg of  $\text{Co}(\text{NO}_3)_2 \cdot 6\text{H}_2\text{O}$ , 51.3 mg of  $\text{Mn}(\text{NO}_3)_2 \cdot 6\text{H}_2\text{O}$ , 20.0 mg of  $\text{IrCl}_4 \cdot x\text{H}_2\text{O}$ , and 30.0 mg of CTAB were dissolved in 20 mL of  $\text{H}_2\text{O}$  to form solution A.

**XAFS measurements.** XAFS spectra at Ir  $L_3$ -edge were obtained at the BL14W1 beamline of Shanghai Synchrotron Radiation Facility (SSRF, Shanghai) operated at 3.5 GeV under ‘top-up’ mode with a constant current of 220 mA. The XAFS data were recorded under fluorescence mode. The energy was calibrated according to the absorption edge of pure Ir foil. XAFS and *in-situ* XAFS spectra at Co  $K$ -edge were obtained at the BL11B beam line of SSRF. The energy was calibrated according to the absorption edge of pure Co foil. Athena software was used to extract the data. XAS spectra at Co  $L$ -edge, Cu  $L$ -edge, and O  $K$ -edge were measured at the beamline BL12B of the National Synchrotron Radiation Laboratory (NSRL, Hefei).

**Electrochemical measurements.** An electrochemical workstation (CHI 660E, Shanghai CH Instruments) was used to measure the electrocatalytic performance of the samples. The electrocatalytic measurements were conducted in a standard three-electrode system at room temperature. The carbon paper ( $1 \times 0.5 \text{ cm}^2$ ) loaded with the as-obtained catalysts ( $2 \text{ mg cm}^{-2}$ ) was used as the working electrode. A carbon rod was used as the counter electrode. A  $\text{Hg}/\text{Hg}_2\text{SO}_4$  electrode was used as the reference electrode. The polarization curves of OER were obtained in 0.1 M  $\text{HClO}_4$  electrolyte, using a linear sweep voltammetry method at a potential range from 1.02 to 1.82 V with a sweep rate of  $5 \text{ mV s}^{-1}$ . The potentials were corrected to compensate for the effect of solution resistance, which were calculated by the following equation:  $E_{iR\text{-corrected}} = E$  (V vs RHE)  $- iR$ , where  $i$  is current, and  $R$  is the uncompensated ohmic electrolyte resistance.



Tafel slope ( $b$ ) was determined by fitting polarization curves data to the Tafel equation:  $\eta = a + b \log |j|$ , where  $\eta$  is the overpotential for the OER, and  $j$  is the current density at the given overpotential. Electrochemical impedance spectroscopy (EIS) measurements were conducted at 1.55 V. The amplitude of the sinusoidal wave was 5 mV. The frequency scan range was 100 kHz-0.01 Hz.

**DFT calculations.** Spin-polarized density-functional theory (DFT) calculations were carried out with Perdew, Burke, and Ernzerhof (PBE) functionals using the Vienna ab initio simulation package (VASP) (38-39). The projector augmented wave (PAW) method was adopted to describe the ions-electrons interaction (40-41). A k-point mesh of  $3 \times 2 \times 1$  was used to sample the Brillouin zones. The kinetic energy cutoff was set to 400 eV for plane-wave expansion. During structural optimizations, the tolerances of total energy and force were set to  $10^{-5}$  eV and 0.05 eV/Å, respectively. To accurately describe the 3d electrons, a correlation energy (U) of 3.0 eV was used for Co and Cu atoms, and 2.0 eV was used for Ir atoms, values that have been tested by previous experimental and theoretical studies (42-44).

**Instrumentations.** XRD patterns were recorded using a Philips X'Pert Pro Super diffractometer with Cu-K $\alpha$  radiation ( $\lambda = 1.54178$  Å). HAADF-STEM images were taken on a JEOL ARM-200F field-emission transmission electron microscope operating at an accelerating voltage of 200 kV using Mo-based TEM grids. EDX elemental mapping images were taken on an FEI Talos F200X high-resolution transmission electron microscope using Mo-based TEM grids. XPS measurements were performed on a Kratos AXIS SUPRA+ with Al K $\alpha$  = 1486.6 eV as the exciting source. ICP-AES (Atomscan Advantage, Thermo Jarrell Ash, USA) analyses were used to determine the mass loadings of Ir single atoms and the dissolved amount of Co species. The distance between Ir single atoms was measured on HAADF-STEM images by Nano Measurer software.

**Data availability.** All data is available in the main text or the supplementary information.

## References

1. S. Hao, et al. Torsion strained iridium oxide for efficient acidic water oxidation in proton

- exchange membrane electrolyzers. *Nat. Nanotechnol.* **16**, 1371-1377 (2021).
2. S. Z. Oener, et al. Accelerating water dissociation in bipolar membranes and for electrocatalysis. *Science* **369**, 1099-1103 (2016).
  3. Y. Wen, et al. Stabilizing highly active Ru sites by suppressing lattice oxygen participation in acidic water oxidation. *J. Am. Chem. Soc.* **143**, 6482-6490 (2021).
  4. L. C. Seitz, et al. A highly active and stable  $\text{IrO}_x/\text{SrIrO}_3$  catalyst for the oxygen evolution reaction. *Science* **353**, 1011-1014 (2016).
  5. A. A. H. Tajuddin, et al. Corrosion-resistant and high-entropic non-noble-metal electrodes for oxygen evolution in acidic media. *Adv. Mater.* **35**, e2207466 (2023).
  6. Z. Y. Wu, et al. Non-iridium-based electrocatalyst for durable acidic oxygen evolution reaction in proton exchange membrane water electrolysis. *Nat. Mater.* **22**, 100-108 (2023).
  7. F. T. Haase, et al. Role of nanoscale inhomogeneities in  $\text{Co}_2\text{FeO}_4$  catalysts during the oxygen evolution reaction. *J. Am. Chem. Soc.* **144**, 12007-12019 (2022).
  8. H. Yang, et al. Intramolecular hydroxyl nucleophilic attack pathway by a polymeric water oxidation catalyst with single cobalt sites. *Nat. Catal.* **5**, 414-429 (2022).
  9. F. T. Haase, et al. Size effects and active state formation of cobalt oxide nanoparticles during the oxygen evolution reaction. *Nat. Energy* **7**, 765-773 (2022).
  10. J. Wang, et al. Redirecting dynamic surface restructuring of a layered transition metal oxide catalyst for superior water oxidation. *Nat. Catal.* **4**, 212-222 (2021).
  11. J. Shan, et al. Short-range ordered iridium single atoms integrated into cobalt oxide spinel structure for highly efficient electrocatalytic water oxidation. *J. Am. Chem. Soc.* **143**, 5201-5211 (2021).
  12. T. Wu, et al. Iron-facilitated dynamic active-site generation on spinel  $\text{CoAl}_2\text{O}_4$  with self-termination of surface reconstruction for water oxidation. *Nat. Catal.* **2**, 763-772 (2019).
  13. L. An, et al. Recent development of oxygen evolution electrocatalysts in acidic environment. *Adv. Mater.* **33**, e2006328 (2021).
  14. F.-Y. Chen, et al. Stability challenges of electrocatalytic oxygen evolution reaction: from mechanistic understanding to reactor design. *Joule* **5**, 1704-1731 (2021).
  15. Z. W. Seh, et al. Combining theory and experiment in electrocatalysis: insights into materials design. *Science* **355**, aad4998 (2017).
  16. M. Chatti, et al. Intrinsically stable in situ generated electrocatalyst for long-term oxidation

- of acidic water at up to 80 °C. *Nat. Catal.* **2**, 457-465 (2019).
17. T. A. Evans, K-S. Choi, Electrochemical synthesis and investigation of stoichiometric, phase-pure CoSb<sub>2</sub>O<sub>6</sub> and MnSb<sub>2</sub>O<sub>6</sub> electrodes for oxygen evolution reaction in acidic media. *ACS Appl. Energy Mater.* **3**, 5563-5571 (2020).
  18. W. H. Lee, et al. Electrode reconstruction strategy for oxygen evolution reaction: maintaining Fe-CoOOH phase with intermediate-spin state during electrolysis. *Nat. Commun.* **13**, 605 (2022).
  19. C. Ye, et al. Activating metal oxides nanocatalysts for electrocatalytic water oxidation by quenching-induced near-surface metal atom functionality. *J. Am. Chem. Soc.* **143**, 14169-14177 (2021).
  20. F. Xing, et al. Ternary platinum-cobalt-indium nanoalloy on ceria as a highly efficient catalyst for the oxidative dehydrogenation of propane using CO<sub>2</sub>. *Nat. Catal.* **5**, 55-65 (2022).
  21. S. Li, et al. Operando revealing dynamic reconstruction of NiCo carbonate hydroxide for high-rate energy storage. *Joule* **4**, 673-687 (2020).
  22. D. He, et al. Active electron density modulation of Co<sub>3</sub>O<sub>4</sub>-based catalysts enhances their oxygen evolution performance. *Angew. Chem. Int. Ed.* **59**, 6929-6935 (2020).
  23. Y. Lu, et al. Tuning the selective adsorption site of biomass on Co<sub>3</sub>O<sub>4</sub> by Ir single atoms for electrosynthesis. *Adv. Mater.* **33**, e2007056 (2021).
  24. W. Guo, et al. Operando leaching of pre-incorporated Al and mechanism in transition-metal hybrids on carbon substrates for enhanced charge storage. *Matter* **4**, 2902-2918 (2021).
  25. P. Ma, et al. Modulating hydrogen bonding in single-atom catalysts to break scaling relation for oxygen evolution. *Chem Catal.* **2**, 2764-2777 (2022).
  26. X. L. Zhang, et al. Strongly coupled cobalt diselenide monolayers for selective electrocatalytic oxygen reduction to H<sub>2</sub>O<sub>2</sub> under acidic conditions. *Angew. Chem. Int. Ed.* **60**, 26922-26931 (2021).
  27. T. C. Chou, et al. Controlling the oxidation state of the Cu electrode and reaction intermediates for electrochemical CO<sub>2</sub> reduction to ethylene. *J. Am. Chem. Soc.* **142**, 2857-2867 (2020).
  28. C. L. Phillips, T. Z. Regier, D. Peak, Aqueous Cu(II)-organic complexation studied in situ using soft X-ray and vibrational spectroscopies. *Environ. Sci. Technol.* **47**, 14290-14297 (2013).

29. Z. Fan, et al. Extraordinary acidic oxygen evolution on new phase 3R-iridium oxide. *Joule* **5**, 3221-3234 (2021).
30. J. Kang, et al. Iridium boosts the selectivity and stability of cobalt catalysts for syngas to liquid fuels. *Chem* **8**, 1050-1066 (2022).
31. C. Feng, et al. Tuning the electronic and steric interaction at the atomic interface for enhanced oxygen evolution. *J. Am. Chem. Soc.* **144**, 9271-9279 (2022).
32. H. Su, et al. In-situ spectroscopic observation of dynamic-coupling oxygen on atomically dispersed iridium electrocatalyst for acidic water oxidation. *Nat. Commun.* **12**, 6118 (2021).
33. B. Zhang, et al. High-valence metals improve oxygen evolution reaction performance by modulating 3d metal oxidation cycle energetics. *Nat. Catal.* **3**, 985-992 (2020).
34. C. Lin, et al. In-situ reconstructed Ru atom array on  $\alpha$ -MnO<sub>2</sub> with enhanced performance for acidic water oxidation. *Nat. Catal.* **4**, 1012-1023 (2021).
35. Z. Shi, et al. Confined Ir single sites with triggered lattice oxygen redox: toward boosted and sustained water oxidation catalysis. *Joule* **5**, 2164-2176 (2021).
36. P. Zhai, et al. Regulating electronic states of nitride/hydroxide to accelerate kinetics for oxygen evolution at large current density. *Nat. Commun.* **14**, 1873 (2023).
37. H. Hu, et al. Construction of complex CoS hollow structures with enhanced electrochemical properties for hybrid supercapacitors. *Chem* **1**, 102-113 (2016).
38. G. Kresse, & J. Furthmüller, Efficient iterative schemes for ab initio total-energy calculations using a plane-wave basis set. *Phys. Rev. B* **54**, 169-186 (1996).
39. J. P. Perdew, K. Bruke, M. Ernzerhof, Generalized gradient approximation made simple. *Phys. Rev. Lett.* **77**, 3865-3868 (1996).
40. P. E. Blochl, et al. Projector augmented-wave method. *Phys. Rev. B* **50**, 17953-17979 (1994).
41. G. Kresse, & D. Joubert, From ultrasoft pseudopotentials to the projector augmented-wave method. *Phys. Rev. B* **59**, 1758-1775 (1999).
42. M. García-Mota, A. Vojvodic, F. Abild-Pedersen, J. K. Nørskov, Electronic origin of the surface reactivity of transition-metal-doped TiO<sub>2</sub>(110). *J. Phys. Chem. C* **117**, 460-465 (2012).
43. X. Li, et al. Design of efficient catalysts with double transition metal atoms on C<sub>2</sub>N layer. *J. Phys. Chem. Lett.* **7**, 1750-1755 (2016).
44. J. Zhou, & Q. Sun, Magnetism of phthalocyanine-based organometallic single porous sheet.

*J. Am. Chem. Soc.* **133**, 15113-15119 (2011).

## **Acknowledgements**

This work was supported by National Key Research and Development Program of China (2021YFA1500500, 2019YFA0405600), CAS Project for Young Scientists in Basic Research (YSBR-051), National Science Fund for Distinguished Young Scholars (21925204), NSFC (U19A2015, 22221003, 22250007, 22202192, 22163002), Collaborative Innovation Program of Hefei Science Center, CAS (2022HSC-CIP004), International Partnership Program of Chinese Academy of Sciences (123GJHZ2022101GC), the DNL Cooperation Fund, CAS (DNL202003), Anhui Natural Science Foundation for Young Scholars (2208085QB52), USTC Research Funds of the Double First-Class Initiative (YD9990002016), and the Guizhou Provincial Science and Technology Projects (QKHJC-ZK[2021]YB047, 2021GZJ001).

## **Author contributions**

Z.Z., S.Z., and **J.Z.** designed the study. P.M., C.F., J.Y., J.H., **J.Z.**, and Z.Z. conducted the experiments. M.Z. conducted HAADF-STEM analysis. C.J. carried out DFT calculations. Z.Z., S.Z., and **J.Z.** wrote the paper. All authors discussed the results and contributed to the manuscript.

<sup>1</sup>Hefei National Research Center for Physical Sciences at the Microscale, Key Laboratory of Strongly-Coupled Quantum Matter Physics of Chinese Academy of Sciences, Key Laboratory of Surface and Interface Chemistry and Energy Catalysis of Anhui Higher Education Institutes, Department of Chemical Physics, University of Science and Technology of China, Hefei, Anhui 230026, P. R. China

<sup>2</sup>Guizhou Provincial Key Laboratory of Computational Nano-Material Science, Institute of Applied Physics, Guizhou Education University, Guiyang, Guizhou 550018, P. R. China

<sup>3</sup>National Synchrotron Radiation Laboratory, Key Laboratory of Precision and Intelligent Chemistry, *iChEM* (Collaborative Innovation Center of Chemistry for Energy Materials), University of Science and Technology of China, Hefei, Anhui 230026, P. R. China



<sup>4</sup>School of Chemistry & Chemical Engineering, Anhui University of Technology, Ma'anshan, Anhui 243002, P. R. China

\*Corresponding author E-mail: zhousm@ustc.edu.cn (S.Z.); zengj@ustc.edu.cn (J.Z.)

<sup>†</sup>These authors contributed equally to this work.

### **Competing interests**

The authors declare no competing interests.